ACS Photonics

Letter

Cite This: ACS Photonics XXXX, XXX, XXX−XXX

pubs.acs.org/journal/apchd5

Tellurene: A Multifunctional Material for Midinfrared Optoelectronics

Skylar Deckoff-Jones,*[,†] Yixiu Wang,[‡] Hongtao Lin,[§] Wenzhuo Wu,[‡] and Juejun Hu*[,†]

[†]Department of Materials Science and Engineering, Massachusetts Institute of Technology, Cambridge, Massachusetts, United States

[‡]School of Industrial Engineering, Purdue University, West Lafayette, Indiana, United States

[§]College of Information Science and Electronic Engineering, Zhejiang University, Zhejiang, China

Supporting Information

ABSTRACT: The mid-infrared spectral band (2−20 μm) is of significant technological importance for thermal imaging, spectroscopic sensing, and free-space communications. Lack of optical materials compatible with common semiconductor substrates, however, presents a standing hurdle for integrated photonic device development in the mid-infrared domain. Tellurene, atomically thin crystals of elemental tellurium, is an emerging 2-D material amenable to scalable solution-based synthesis. It uniquely combines small and tunable bandgap energies, high carrier mobility, exceptionally large electro-optic activity, and superior chemical stability, making it a promising and versatile material platform for mid-infrared photonics. With these material properties in mind, we propose and design a waveguide-integrated tellurene photodetector and Pockels effect modulator. The photodetector boasts a record room temperature noise equivalent power of 0.03 fW/Hz$^{1/2}$ at 3 μm wavelength, while the optimized modulator device claims a half-wave voltage-length product ($V_\pi \cdot L$) of 2.7 V·cm and a switching energy of 12.0 pJ/bit, both representing substantial improvements to current state-of-the-art devices.

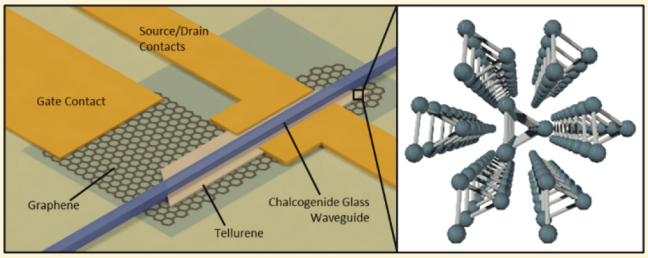

KEYWORDS: *tellurium, electro-optics, chalcogenide glass, Pockels effect, photodetector, modulator*

Recent advances exploiting the extraordinary electronic and optical properties of 2-D materials have led to new device paradigms for next-generation integrated photonics. However, roadblocks exist for known 2-D van der Waals (vdW) layered materials to meet the emerging technological needs of mid-IR integrated photonics. For instance, the zero bandgap nature of graphene results in low gating modulation and high dark carrier concentrations, limiting its application for photodetectors. Additionally the poor chemical stability of black phosphorus or black arsenic phosphorus limits their compatibility with standard photonic integration and device lifetime.[1,2]

The recently demonstrated solution synthesis of tellurene with high throughput and quality shows great promise as an alternative for mid-IR integrated optoelectronics.[3−5] The synthesized free-standing tellurene crystals have large lateral dimensions (from tens to hundreds of microns) and process-controlled thickness (from a monolayer to tens of nanometers). All tellurene flakes grow laterally along the ⟨0001⟩ and ⟨$1\bar{2}10$⟩ directions, with the vertical stacking along the ⟨$10\bar{1}0$⟩ directions. Tellurene offers several critical materials and processing advantages for mid-IR integrated photonics: (1) tellurene has a thickness-dependent bandgap (∼0.35−1.2 eV) covering mid-IR bands up to 3.5 μm wavelength;[6,7] (2) it boasts excellent gating modulation on/off ratio (∼10^5−10^6) and can be depleted by applying an electric field, a critical feature for reducing dark current in photodetectors and power consumption in our modulator design due to Joule heating; (3) tellurene is air-stable without encapsulation at ambient conditions; (4) tellurene's chain structure leads to the existence of the dangling bonds, only at the (0001) ends of the molecular chains, so edge recombination will most likley only occur at the [0001] edges, thereby ensuring long carrier lifetime; and (5) tellurene can be scalably produced via low-cost, substrate-free solution processing and assembled over large areas using a Langmuir−Blodgett (LB) process with predefined crystalline lattice orientations, enabling the proposed devices and future explorations of tellurene on diverse designer substrates.[8]

Tellurene synthesized following the solution route has recently been utilized to fabricate free-space photoconductive detectors with an already impressive room-temperature peak noise-equivalent power (NEP) of 0.28 pW/Hz$^{1/2}$ at 1.7 μm wavelength.[9] This initial demonstration corroborates the high optoelectronic quality of tellurene processed using the solution technique. In this work, we investigate waveguide integration of mid-IR tellurene detectors. In addition to the apparent advantage of facilitating on-chip integration, waveguide

Received: May 13, 2019
Published: June 27, 2019

DOI: 10.1021/acsphotonics.9b00694
ACS Photonics XXXX, XXX, XXX−XXX

integration also introduces several important performance benefits. First, the longer path length made possible by waveguide integration contributes to enhanced optical absorption. This benefit is particularly pronounced if we are to extend the spectral range of the detector to the mid-IR (2−3.6 μm), where response of the free space detector prototype significantly rolls off due to attenuated absorption.[9] Moreover, waveguide integration improves the signal-to-noise ratio (SNR). When light is funneled into the detector via a waveguide (with a core index n) rather than from free space, the detector active volume and hence noise can be reduced approximately by a factor of n^2.[10] Since most detector noises (Johnson, generation-recombination, and shot noises) scale with active volume,[11] the size scaling leads to suppressed noise. Finally, waveguide-integrated detectors can attain larger bandwidth than their free space counterparts thanks to their diminished RC delay and carrier transit time.

In addition to photodetectors, optical modulators and switches are vital components of a photonic circuit to enable signal switching and routing, data encoding, phase-sensitive detection, and spectroscopic interrogation.[12,13] Mid-IR modulators have attracted significant interests in recent years, and several modulator technologies have been developed in the mid-IR regime using thermo-optic phase shift,[14−16] free carrier plasma dispersion,[17,18] electro-absorption (Pauli blocking or field-induced effects),[19−21] or electro-refractive (Pockels) effect.[22] Among them, Pockels electro-optic (EO) modulators are particularly attractive given their intrinsic ultrafast response (>THz) and the capacity of achieving phase-only modulation, an important characteristic enabling scalable optical switching. To date, mid-IR integrated Pockels modulators have only been experimentally implemented in Si-on-$LiNbO_3$[22] and theoretically analyzed in AlN-on-SiO_2.[23] The designs mandate hybrid integration on less-standard substrates, operate over a limited mid-IR band (<5 μm) bound by phonon absorption in the oxides, and demand high driving voltages (>50 V) due to low EO activity in the materials.

2-D materials have demonstrated singular nonlinear optical properties.[24] In particular, the transition metal chalcogenides (TMDC) exhibit very strong second harmonic generation (large $\chi^{(2)}$), but only for few-layer thicknesses where the inversion symmetry of the crystal structure is broken.[25] This unfortunately limits their use for EO modulators, as the optical modal overlap with the electro-optic material would be too low for efficient modulation. Tellurene features extraordinary EO activity even as a bulk material, which makes it a superb candidate for mid-IR Pockels effect modulators. Bulk tellurium exhibits a large linear EO coefficient d_{11} = 44.2 pm/V.[26] The refractive index change due to Pockels effect is given by

$$\Delta n_{EO} = -\frac{1}{2} n_{EO}^3 d_{11} E \quad (1)$$

where n_{EO} is the refractive index of the EO material (Te), d_{11} is the EO tensor element, and E is the applied electric field.[9] In addition to its large EO coefficient, tellurene's high refractive index of 5 along the ordinary axis further enhances its EO activity according to eq 1: the EO activity of tellurene is 90× larger than that of the gold standard EO material $LiNbO_3$![27,28]

Set aside its extraordinary EO activity, tellurene is also fundamentally different from traditional EO crystals in that it is a semiconductor rather than an electrical insulator, and thus, motion of free carriers under applied bias significantly alters the device behavior. We note that this challenge is not unique to tellurene: strained Si is another semiconducting EO material potentially with tremendous technological importance. So far, EO devices utilizing strained Si have adopted an insulator−semiconductor−insulator (ISI) configuration (effectively two back-to-back MOS structures).[29−31] In this configuration, the applied electric field is heavily screened by the free carriers in Si, resulting in severely reduced Pockels effect. In fact, more recent studies have found that the earlier reports substantially overestimates the Pockels contribution from strained Si in these devices, and the observed second-order EO response mostly derives from free carrier and interface effects.[32−35] In this paper we propose a simple and effective design to counter the free carrier screening issue by operating the device in a resistive mode. In addition to achieving excellent performance with tellurene-based mid-IR modulators, the design can also utilize new semiconductor EO materials for optical modulation and switching over diverse spectral bands.

CHALCOGENIDE GLASS-ON-TELLURENE DESIGN PLATFORM

The tellurene photodetector and modulator designs are based on the chalcogenide glass-on-2D-material platform, which we recently demonstrated.[36,37] This platform leverages chalcogenide glasses (ChGs), amorphous compounds containing S, Se, or Te, to enable direct fabrication of integrated photonic devices on 2-D vdW materials. Unlike the traditional approach where exfoliated or delaminated 2-D crystals are transferred onto prefabricated devices, ChG films are directly grown on 2-D materials at room temperature and lithographically patterned into devices, allowing for high-throughput, high-yield device processing and accurate alignment to crystallographic axes. We further found that ChG thin films can act as an effective passivation layer to prevent degradation of 2-D materials due to oxygen and moisture in the ambient environment, while maintaining their exceptional optoelectronic properties.

The integration scheme and the tellurene material constitute a highly complementary combination offering several benefits. First, the broad mid-IR transparency window of ChGs nicely match the operation bands of the tellurene devices (up to 3.5 μm for detectors and above 3.5 μm for modulators). Specifically, the two target glasses $Ge_{23}Sb_7S_{70}$ (GeSbS, n = 2.1, transparent up to 11 μm) and $Ge_{23}Sb_7Se_{70}$ (GeSbSe, n = 2.7, transparent up to 16 μm) provide sufficient index contrast for light guiding and can both be deposited monolithically on tellurene. The $Ge_{23}Sb_7S_{70}$ glass can also serve as an infrared-transparent gate dielectric for modulating carrier concentrations in tellurene without involving optically absorbing oxides.[37] In addition, the ability to custom design and precisely align photonic devices to specific crystalline orientations of tellurene crystals is critical, given the in-plane anisotropy of photoresponse and EO activity in tellurene. Finally, solution-processed tellurene represents a salient example of 2-D materials that can potentially be assembled over large areas and on different substrates.[38] The ChG-on-tellurene platform therefore heralds a truly monolithic, wafer-scale integration process of mid-IR photonics on standard substrates facilitating scalable manufacturing of mid-IR optical systems.

DOI: 10.1021/acsphotonics.9b00694
ACS Photonics XXXX, XXX, XXX−XXX

ROOM-TEMPERATURE HIGH-PERFORMANCE MID-IR TELLURENE PHOTODETECTOR

Figure 1a depicts the waveguide-integrated photoconductive detector design consisting of a graphene bottom gate and a ChG waveguide on tellurene. The bottom gate is used to modulate the carrier concentration in Te to minimize dark current and also prohibit premature long wavelength cutoff due to Pauli blocking. The waveguide is aligned along the [0001] axis, a choice that contributes to extended operation spectral ranges given the in-plane optical absorption anisotropy of tellurene.[9] The detector is optimized to maximize its noise equivalent power (NEP), the figure-of-merit giving the signal-to-noise ratio of waveguide-integrated photodetectors.[39] Specifically, the design is based on these considerations: (1) the tellurene thickness is chosen such that it can be fully depleted with gating while maintaining sufficient modal confinement; (2) given the tellurene thickness, the waveguide dimensions are determined to ensure single-mode operation and minimize coupling loss into Te; (3) the detector length is optimized by considering the trade-off between dark current (which linearly scales with detector length) and optical absorption; and (4) the metal contact spacing is chosen to balance responsivity and parasitic absorption. More details on these optimizations can be found in the Supporting Information. Minimum carrier concentrations in the gated tellurene were simulated by numerically solving the steady-state carrier distribution in the layer stack (see Supporting Information, Figure S2-S1). Figure 1b shows the minimum achievable carrier concentration in the graphene/$Ge_{23}Sb_7S_{70}$ (20 nm)/tellurene metal−insulator−semiconductor (MIS) structure. In this MIS structure, the $Ge_{23}Sb_7S_{70}$ and graphene serve as a mid-IR transparent gate dielectric and electrode, respectively.[37] A minimum carrier concentration of 7.5×10^{15} cm^{-3} can be achieved for 10 nm thick tellurene. Thicknesses below 10 nm are undesirable for photodetectors, as the bandgap will begin to increase, limiting the spectral range of the detector.

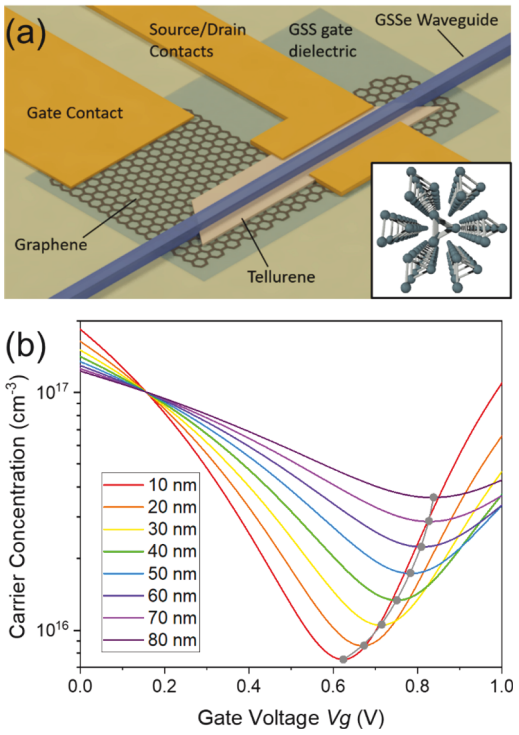

Figure 1. (a) Schematic of waveguide integrated tellurene photodetector. Inset shows view of tellurene crystal structure along [0001] axis. (b) Simulated effective carrier concentration for different gate voltages in tellurene flakes of different thicknesses. The dotted gray line connects the minimum achievable carrier concentration for each thickness.

Figure 2a shows the side-view optical intensity distribution in a detector simulated using 3-D finite-difference time-domain (FDTD) based on measured material optical constants.[9] The design is optimized following the aforementioned procedures. Coupling into the tellurene absorber is highly efficient given the small tellurium thickness compared to the waveguide height (700 nm), which maintains an optical scattering loss at the flake edge below 0.1 dB from the modal mismatch (Figure 2b,c). Waveguide dimensions were chosen to allow single mode detection up to 3.5 μm. Using experimentally measured data of solution-synthesized tellurene (mobility along the [1$\bar{2}$10] axis: 240 cm^2 V^{-1} s^{-1}; carrier density: 10^{11} cm^{-2}; photocarrier lifetime: 280 ns[40]), we can project the optimized NEP of the preliminary detector design to be 0.03 fW/$Hz^{1/2}$ at

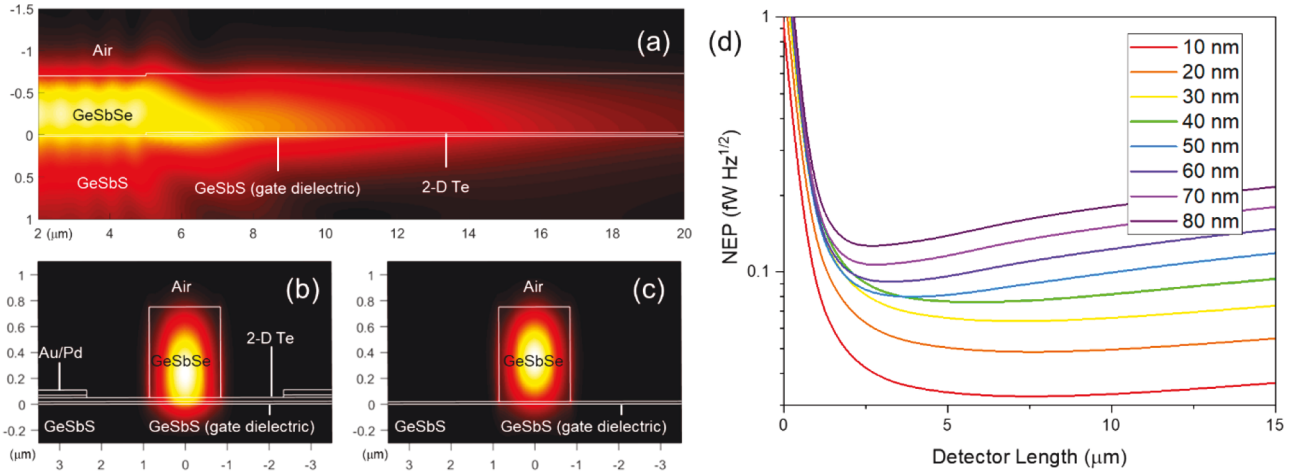

Figure 2. (a) Simulated optical intensity distribution in a waveguide-coupled 30 nm thick tellurene mid-IR detector; (b, c) mode profiles inside the ChG waveguide (b) with and (c) without tellurene; (d) computed NEP of the detector as a function of the device length and tellurene thickness.

DOI: 10.1021/acsphotonics.9b00694
ACS Photonics XXXX, XXX, XXX−XXX

3 μm wavelength (see Supporting Information for details on NEP calculation). As can be seen from Figure 2d, this NEP value corresponds to an optimal device length to balance between sufficiently large optical absorption and a small detector length with reduced dark current. Furthermore, thinner tellurene allows for lower NEP because of its reduced dark current, despite its weaker absorption. The photodetector bandwidth is dictated by the carrier lifetime and RC bandwidth given by

$$f_{3dB} = \frac{1}{2\pi\sqrt{RC^2 + \tau^2}} \quad (2)$$

where τ is the photocarrier lifetime, which limits the bandwidth to be 0.57 MHz, comparable to other mid-IR photoconductive detectors.[41] Such performance, represents almost 4 orders of magnitude improvement in SNR compared to the free-space counterpart.[9] The NEP value is also far superior to the best figure previously reported for mid-IR waveguide-integrated detectors (35 fW/Hz$^{1/2}$ in an InP-based multiquantum-well detector hybrid bonded on Si[42,43]), while our device further claims the benefits of simple processing and fully monolithic integration on most substrates. The superior performance and Si-monolithic integration capacity qualify the tellurene device as a promising solution for mid-IR detection on-chip.

POCKELS EFFECT MODULATOR

Tellurene exhibits strong anisotropy along the two principle in-plane directions ([0001] and [1$\bar{2}$10]) due to its low-symmetry lattice, a factor that must be properly considered in Pockels device design. To appropriately engineer a tellurene-based EO modulator, we experimentally characterized anisotropy of tellurene's second-order nonlinear susceptibility tensor by measuring second harmonic generation (SHG) from solution-derived tellurene flakes using multiphoton microscopy. The tellurene was prepared by placing 0.01 g analytical-grade Na_2TeO_3 and 0.5 g polyvinylpyrrolidone (PVP) into a 50 mL Teflon-lined stainless-steel autoclave. Then, 33 mL of double-distilled water was poured into the autoclave under magnetic stirring to form a homogeneous solution. After that, 3.5 mL of ammonia solution and 1.75 mL of hydrazine hydrate were filled into the above solution. The autoclave was sealed and maintained at 180 °C for 30 h. In the end, the autoclave was cooled to room temperature naturally. The resulting solid silver-gray products were precipitated by centrifugation at 5000 rpm for 5 min and washed three times with distilled water. The SHG measurments were done on a Zeiss LSM880 NLO Multiphoton Microscope. Figure 3a,b shows the reflected fundamental (1300 nm) and SHG (650 nm) of multiple tellurene flakes of different sizes and orientations. The tellurene crystals that have their [0001] direction vertical to the images (perpendicular to the fundamental polarization), demonstrate the most intense SHG. Tellurene's structure belongs to the D_3 point group resulting in five nonvanishing second-order susceptibility tensor elements. Figure 3c shows the intensity of the second harmonic as a function of the relative angle between the tellurene flakes and the laser polarization. The cosine squared fit agrees with the D_3 symmetry of tellurene. Knowing the orientation of the electric field relative to the tellurene's crystalline orientation, the change in the refractive index of the tellurene under the applied field can be calculated. Figure 3d shows how the refractive index of tellurene changes as the angle between the

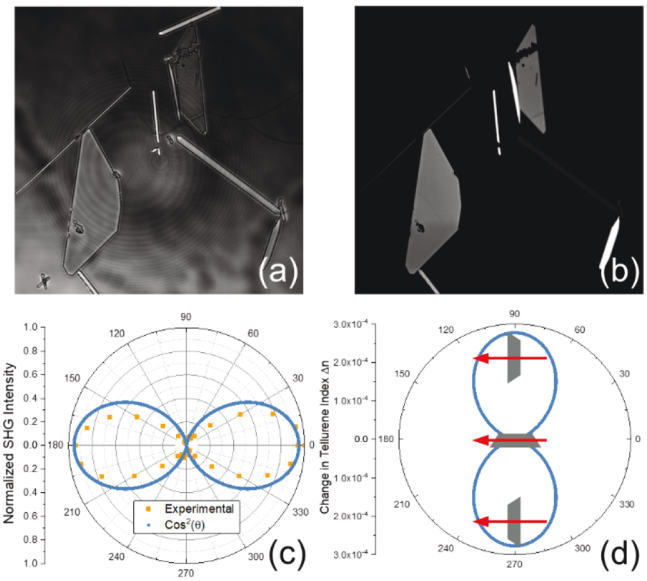

Figure 3. (a) Multiphoton microscope image of reflected 1300 nm fundamental beam (b) and 650 nm reflected SHG. Fundamental laser polarization is horizontal. (c) SHG intensity from tellurene samples as a function of incident laser polarization. The experimental data fit well to a cosine squared function, in agreement with tellurium's crystal structure; (d) change in refractive index of tellurium as a function of the angle between the [0001] direction and an electric field of 10^3 V/cm. Insets show the orientation of tellurene (gray trapezoid) relative to electric field (red arrow) for the orientations corresponding to maximum and minimum change in refractive index.

applied electric field and [0001] direction changes. The result indicates that the waveguide should align along the [0001] axis of tellurene, while the contacts adjacent to the waveguide will produce an electric field perpendicular to the [0001] direction to attain the maximum EO response.

Following the conclusion, the Pockels EO phase shifter layout is similar to that of the waveguide-integrated photodetector shown in Figure 1a. Instead of using an ISI structure, here the metal electrodes directly contact the tellurene. Pd/Au contacts are used because Pd has been demonstrated to have a low contact resistance with tellurene.[38] Voltage drop takes place almost entirely in tellurene, since the Pd electrode contact resistance (6 Ω) is much smaller than tellurene's resistance (719 Ω for 80 nm thick tellurene). The gate serves two purposes: by biasing the gate such that tellurene operates near the onset of inversion, the electrical resistance is maximized to increase the electric field in tellurene; additionally, electric current passing through tellurene and, hence, power consumption of the device are also minimized according to the classical Ohm's law.

The phase shifter design is optimized to minimize the half-wave voltage-length product ($V_\pi \cdot L$) and power consumption. The product $V_\pi \cdot L$ is primarily dictated by the spatial overlap between the optical mode (at 4 μm wavelength in our initial design) and the electric field in the EO medium. Figure 4a,b presents the simulated cross-sectional electric and optical field distribution in the EO phase shifter, showing large overlap between the fields in tellurene. The ChG waveguide size is chosen to be 2.5 μm × 0.71 μm to maximize confinement factor (see Supporting Information, Figure S7-S5). Spatially dependent EO index modification Δn_{EO} is then computed

DOI: 10.1021/acsphotonics.9b00694
ACS Photonics XXXX, XXX, XXX−XXX

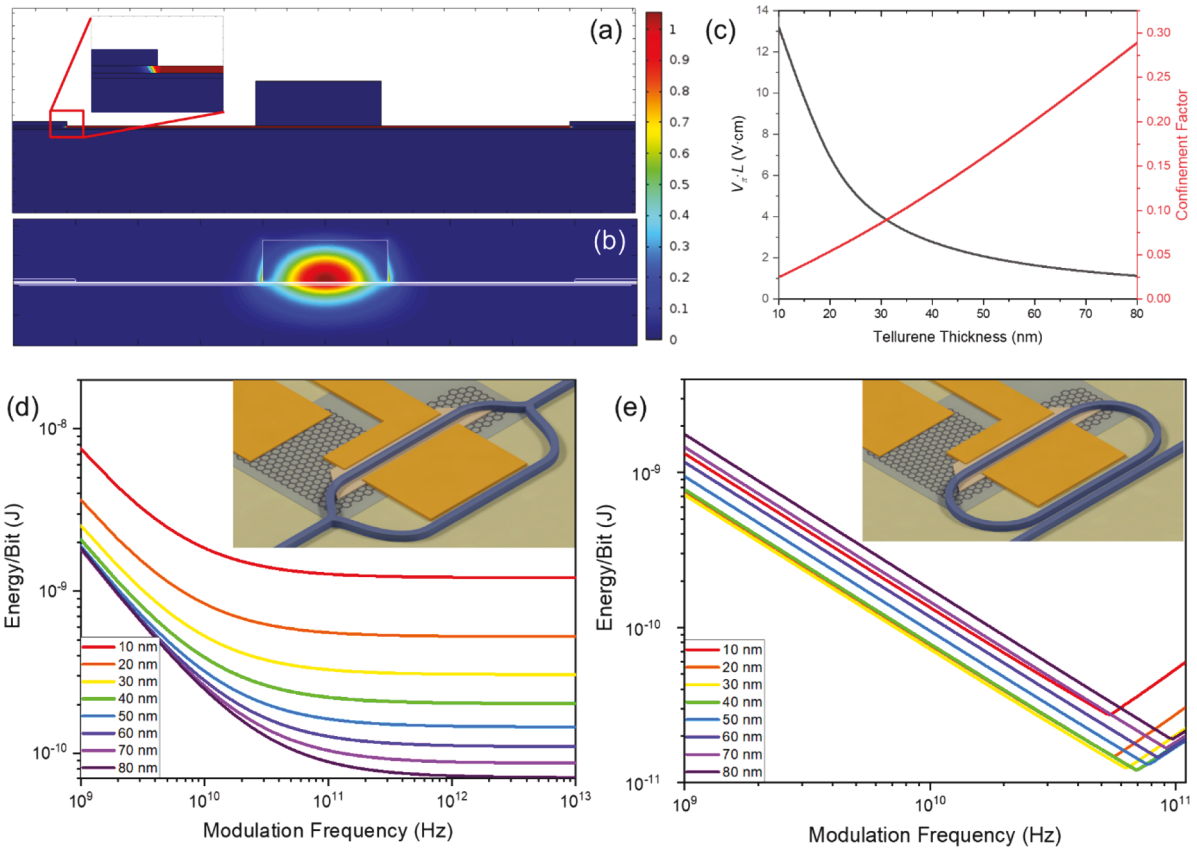

Figure 4. (a, b) Simulated cross-sectional (a) electric and (b) optical field profiles in the modulator. (c) Simulated confinement factor and voltage-length product for different tellurene thicknesses. (d) Simulated energy consumption of the modulator vs frequency for different 2-D Te thicknesses in MZI architecture tellurene modulator. Inset shows schematic of MZI modulator design (e) Simulated energy consumption of tellurene racetrack modulator vs frequency for different tellurene thickness. Inset shows schematic of racetrack modulator design.

using eq 1, and the waveguide effective index modulation is derived following the classical perturbation theory:[12,44]

$$\Delta n_{\text{eff}} = \frac{n_{\text{EO}} c_0 \varepsilon_0 \iint_{\text{EO}} \Delta n_{\text{EO}} |E|^2 \, dx dy}{\iint_{\infty} \text{Re}(E \times H^*) \cdot \hat{z} \cdot dx dy} \tag{3}$$

where c_0 and ε_0 denote light speed and permittivity in vacuum, and E and H represent the optical modal fields. The integral in the numerator is performed across the EO material whereas the one in the denominator is integrated over the entire waveguide cross-section. This approach allows us to quantify the $V_\pi \cdot L$ product for varying thickness of tellurene. According to the simulation results shown in Figure 4c, $V_\pi \cdot L$ improves with increasing tellurene thickness benefiting from enhanced optical modal overlap, although the performance gain plateaus at larger tellurene thicknesses. At 40 nm tellurene thickness, the optimized $V_\pi \cdot L$ reaches 2.7 V·cm, representing a 10-fold improvement compared to state-of-the-art mid-IR EO modulators.[22] The superior $V_\pi \cdot L$ product of the EO phase shifter facilitates its integration in modulator devices with a compact footprint.

Unlike the traditional ISI configuration, where the phase shifter is a purely capacitive device (when leakage current is negligible), a distinctive feature of the new design is its resistive nature, similar to thermo-optic phase shifters. The phase shifter therefore continuously draws electrical power due to Joule heating. The power consumption of a modulator device based on the phase shifter design therefore encompasses both the continuous current flow and capacitive charging/discharging. We analyze the power consumption of a tellurene modulator assuming Mach−Zehnder interferometer (MZI, Figure 4d, inset) and racetrack resonator (Figure 4e, inset) configurations, both based on the phase shifter design. Figure 4d and e plot the modulation energy-per-bit of the two configurations, respectively, for different thicknesses of tellurene. In the calculations, we account for the impact of modal overlap with tellurene, optical scattering loss at the tellurene waveguide interface, as well as the photon lifetime limit to modulation bandwidth. More details of the calculations are furnished in the Supporting Information. Resonators incorporating thinner flakes have higher Q-factors and lower photon-lifetime-limited bandwidth as a result of reduced scattering losses at the waveguide tellurene interfaces. The energy of the devices begins to rapidly increase beyond their photon-lifetime limited bandwidthdue to the increased voltages necessary to drive the device at the same extinction.[45]Their higher Q-factors also lead to a smaller switching bias and lower energy per bit. Competing with both of these factors is the smaller modal overlap with the tellurene for thinner flakes resulting in a smaller $V_\pi \cdot L$. Ultimately, an optimized energy per bit of 12.0 pJ at 70 GHz modulation bandwidth can be achieved in 40 nm tellurene. This is attained in spite of the unfavorable λ^2 (wavelength squared) scaling of the $V_\pi \cdot L$ product for EO modulators. The result indicates that the resistive EO modulator design can overcome the free carrier screening issue while offering competitive performance in terms of energy consumption.

DOI: 10.1021/acsphotonics.9b00694
ACS Photonics XXXX, XXX, XXX−XXX

CONCLUSION

This work demonstrates the promise of tellurene as a multifunctional material for integrated optoelectronic devices in the mid-IR. Tellurene's small bandgap and low gated carrier concentration enable extremely low noise photodetector at room temperature. Additionally, tellurene's broken structural inversion symmetry and giant electrooptic activity allow it to be employed for extremely fast and low energy Pockels effect modulators. Both detector and modulator devices achieve performances orders of magnitude better compared to existing state-of-the-art. The capability of scalable synthesis and assembly of tellurene on arbitrary substrates at low temperatures further facilitates its integration with functional integrated photonic circuits. We therefore foresee that tellurene will become a powerful and versatile material platform for mid-IR optoelectronic applications.

ASSOCIATED CONTENT

Supporting Information

The Supporting Information is available free of charge on the ACS Publications website at DOI: 10.1021/acsphotonics.9b00694.

Details on carrier concentration simulations, effects of mode polarization, details on photodetector optimization, noise calculations, and energy consumption calculations (PDF)

AUTHOR INFORMATION

Corresponding Authors

*E-mail: sdeckoff@mit.edu.
*E-mail: hujuejun@mit.edu.

ORCID

Skylar Deckoff-Jones: 0000-0002-3786-6276
Wenzhuo Wu: 0000-0003-0362-6650

Notes

The authors declare no competing financial interest.

ACKNOWLEDGMENTS

This material is based on work supported by the National Science Foundation under Award Nos. 1453218 and 1506605 and a Graduate Research Fellowship under Grant No. 1122374. The synthesis of tellurene materials is supported by the National Science Foundation under Grant CMMI-1762698. The authors also acknowledge facility support by the Harvard University Center for Nanoscale Systems, the latter of which is supported by the National Science Foundation under Award No. 0335765.

REFERENCES

(1) Kim, S.; Lee, J. Y.; Lee, C. H.; Lee, G. H.; Kim, J. Recovery of the Pristine Surface of Black Phosphorus by Water Rinsing and Its Device Application. *ACS Appl. Mater. Interfaces* **2017**, *9*, 21382−21389.

(2) Liu, B.; Köpf, M.; Abbas, A. N.; Wang, X.; Guo, Q.; Jia, Y.; Xia, F.; Weihrich, R.; Bachhuber, F.; Pielnhofer, F.; et al. Black Arsenic-Phosphorus: Layered Anisotropic Infrared Semiconductors with Highly Tunable Compositions and Properties. *Adv. Mater.* **2015**, *27*, 4423−4429.

(3) Wang, Y.; Qiu, G.; Wang, R.; Huang, S.; Wang, Q.; Liu, Y.; Du, Y.; Goddard, W. A.; Kim, M. J.; Xu, X.; et al. Field-Effect Transistors Made from Solution-Grown Two-Dimensional Tellurene. *Nat. Electron.* **2018**, *1*, 228−236.

(4) Wu, W.; Qiu, G.; Wang, Y.; Wang, R.; Ye, P. Tellurene: Its Physical Properties, Scalable Nanomanufacturing, and Device Applications. *Chem. Soc. Rev.* **2018**, *47*, 7203−7212.

(5) Wang, Y.; de Souza Borges Ferreira, R.; Wang, R.; Qiu, G.; Li, G.; Qin, Y.; Ye, P. D.; Sabbaghi, A.; Wu, W. Data-Driven and Probabilistic Learning of the Process-Structure-Property Relationship in Solution-Grown Tellurene for Optimized Nanomanufacturing of High-Performance Nanoelectronics. *Nano Energy* **2019**, *57*, 480−491.

(6) Zhu, Z.; Cai, X.; Yi, S.; Chen, J.; Dai, Y.; Niu, C.; Guo, Z.; Xie, M.; Liu, F.; Cho, J.-H.; et al. Multivalency-Driven Formation of Te-Based Monolayer Materials: A Combined First-Principles and Experimental Study. *Phys. Rev. Lett.* **2017**, *119*, 106101.

(7) Coker, A.; Lee, T.; Das, T. P. Investigation of the Electronic Properties of Tellurium—Energy-Band Structure. *Phys. Rev. B: Condens. Matter Mater. Phys.* **1980**, *22*, 2968−2975.

(8) Tao, A. R.; Huang, J.; Yang, P. Langmuir-Blodgettry of Nanocrystals and Nanowires. *Acc. Chem. Res.* **2008**, *41*, 1662−1673.

(9) Amani, M.; Tan, C.; Zhang, G.; Zhao, C.; Bullock, J.; Song, X.; Kim, H.; Shrestha, V. R.; Gao, Y.; Crozier, K. B.; et al. Solution-Synthesized High-Mobility Tellurium Nanoflakes for Short-Wave Infrared Photodetectors. *ACS Nano* **2018**, *12*, 7253−7263.

(10) Lin, H.; Luo, Z.; Gu, T.; Kimerling, L. C.; Wada, K.; Agarwal, A.; Hu, J. Mid-Infrared Integrated Photonics on Silicon: A Perspective. *Nanophotonics* **2017**, *7*, 393−420.

(11) Dereniak, E. L.; Boreman, G. D. *Infrared Detectors and Systems*; Wiley, 1996.

(12) Kita, D. M.; Lin, H.; Agarwal, A.; Richardson, K.; Luzinov, I.; Gu, T.; Hu, J. On-Chip Infrared Spectroscopic Sensing: Redefining the Benefits of Scaling. *IEEE J. Sel. Top. Quantum Electron.* **2017**, *23*, 340−349.

(13) Kita, D. M.; Miranda, B.; Favela, D.; Bono, D.; Michon, J.; Lin, H.; Gu, T.; Hu, J. High-Performance and Scalable on-Chip Digital Fourier Transform Spectroscopy. *Nat. Commun.* **2018**, *9*, 4405.

(14) Zou, Y.; Chakravarty, S.; Chung, C.-J.; Chen, R. T. Miniature Mid-Infrared Thermooptic Switch with Photonic Crystal Waveguide Based Silicon-on-Sapphire Mach−Zehnder Interferometers. *Proc. SPIE* **2016**, *9753*, 97530Q.

(15) Malik, A.; Dwivedi, S.; Van Landschoot, L.; Muneeb, M.; Shimura, Y.; Lepage, G.; Van Campenhout, J.; Vanherle, W.; Van Opstal, T.; Loo, R.; et al. Ge-on-Si and Ge-on-SOI Thermo-Optic Phase Shifters for the Mid-Infrared. *Opt. Express* **2014**, *22*, 28479.

(16) Nedeljkovic, M.; Stankovic, S.; Mitchell, C. J.; Khokhar, A. Z.; Reynolds, S. A.; Thomson, D. J.; Gardes, F. Y.; Littlejohns, C. G.; Reed, G. T.; Mashanovich, G. Z. Mid-Infrared Thermo-Optic Modulators in SoI. *IEEE Photonics Technol. Lett.* **2014**, *26*, 1352−1355.

(17) Shen, L.; Healy, N.; Mitchell, C. J.; Penades, J. S.; Nedeljkovic, M.; Mashanovich, G. Z.; Peacock, A. C. Mid-Infrared All-Optical Modulation in Low-Loss Germanium-on-Silicon Waveguides. *Opt. Lett.* **2015**, *40*, 268.

(18) Van Camp, M. A.; Assefa, S.; Gill, D. M.; Barwicz, T.; Shank, S. M.; Rice, P. M.; Topuria, T.; Green, W. M. J. Demonstration of Electrooptic Modulation at 2165nm Using a Silicon Mach-Zehnder Interferometer. *Opt. Express* **2012**, *20*, 28009.

(19) Yao, Y.; Shankar, R.; Kats, M. A.; Song, Y.; Kong, J.; Loncar, M.; Capasso, F. Electrically Tunable Metasurface Perfect Absorbers for Ultrathin Mid-Infrared Optical Modulators. *Nano Lett.* **2014**, *14*, 6526−6532.

(20) Peng, R.; Khaliji, K.; Youngblood, N.; Grassi, R.; Low, T.; Li, M. Midinfrared Electro-Optic Modulation in Few-Layer Black Phosphorus. *Nano Lett.* **2017**, *17*, 6315−6320.

(21) Whitney, W. S.; Sherrott, M. C.; Jariwala, D.; Lin, W.-H.; Bechtel, H. A.; Rossman, G. R.; Atwater, H. A. Field Effect Optoelectronic Modulation of Quantum-Confined Carriers in Black Phosphorus. *Nano Lett.* **2017**, *17*, 78−84.

(22) Chiles, J.; Fathpour, S. Mid-Infrared Integrated Waveguide Modulators Based on Silicon-on-Lithium-Niobate Photonics. *Optica* **2014**, *1*, 350.

DOI: 10.1021/acsphotonics.9b00694
ACS Photonics XXXX, XXX, XXX−XXX

(23) Liu, S.; Xu, K.; Song, Q.; Cheng, Z.; Tsang, H. Design of Mid-Infrared Electro-Optic Modulators Based on Aluminum Nitride Waveguides. *J. Lightwave Technol.* **2016**, 1.
(24) Autere, A.; Jussila, H.; Dai, Y.; Wang, Y.; Lipsanen, H.; Sun, Z. Nonlinear Optics with 2D Layered Materials. *Adv. Mater.* **2018**, *30*, 1705963.
(25) Li, Y.; Rao, Y.; Mak, K. F.; You, Y.; Wang, S.; Dean, C. R.; Heinz, T. F. Probing Symmetry Properties of Few-Layer MoS2 and h-BN by Optical Second-Harmonic Generation. *Nano Lett.* **2013**, *13*, 3329−3333.
(26) Jerphagnon, J. Contribution a L'étude de Certains Phénomènes D'optique Non Linéaire. *Ann. des Télécommunications* **1968**, *23*, 203−232.
(27) Caldwell, R. S.; Fan, H. Y. Optical Properties of Tellurium and Selenium. *Phys. Rev.* **1959**, *114*, 664.
(28) Amani, M.; Tan, C.; Zhang, G.; Zhao, C.; Bullock, J.; Song, X.; Kim, H.; Raj Shrestha, V.; Gao, Y.; Crozier, K. B.; et al. Solution-Synthesized High-Mobility Tellurium Nanoflakes for Short-Wave Infrared Photodetectors. *ACS Nano* **2018**, *12*, 7253−7263.
(29) Chmielak, B.; Waldow, M.; Matheisen, C.; Ripperda, C.; Bolten, J.; Wahlbrink, T.; Nagel, M.; Merget, F.; Kurz, H. Pockels Effect Based Fully Integrated, Strained Silicon Electro-Optic Modulator. *Opt. Express* **2011**, *19*, 17212.
(30) Jacobsen, R. S.; Andersen, K. N.; Borel, P. I.; Fage-Pedersen, J.; Frandsen, L. H.; Hansen, O.; Kristensen, M.; Lavrinenko, A. V.; Moulin, G.; Ou, H.; et al. Strained Silicon as a New Electro-Optic Material. *Nature* **2006**, *441*, 199−202.
(31) Damas, P.; Le Roux, X.; Le Bourdais, D.; Cassan, E.; Marris-Morini, D.; Izard, N.; Maroutian, T.; Lecoeur, P.; Vivien, L. Wavelength Dependence of Pockels Effect in Strained Silicon Waveguides. *Opt. Express* **2014**, *22*, 22095.
(32) Cazzanelli, M.; Schilling, J. Second Order Optical Nonlinearity in Silicon by Symmetry Breaking. *Appl. Phys. Rev.* **2016**, *3*, 011104.
(33) Borghi, M.; Mancinelli, M.; Merget, F.; Witzens, J.; Bernard, M.; Ghulinyan, M.; Pucker, G.; Pavesi, L. High-Frequency Electro-Optic Measurement of Strained Silicon Racetrack Resonators. *Opt. Lett.* **2015**, *40*, 5287.
(34) Sharif Azadeh, S.; Merget, F.; Nezhad, M. P.; Witzens, J. On the Measurement of the Pockels Effect in Strained Silicon. *Opt. Lett.* **2015**, *40*, 1877.
(35) Schriever, C.; Bianco, F.; Cazzanelli, M.; Ghulinyan, M.; Eisenschmidt, C.; de Boor, J.; Schmid, A.; Heitmann, J.; Pavesi, L.; Schilling, J. Second-Order Optical Nonlinearity in Silicon Waveguides: Inhomogeneous Stress and Interfaces. *Adv. Opt. Mater.* **2015**, *3*, 129−136.
(36) Deckoff-Jones, S.; Lin, H.; Kita, D.; Zheng, H.; Li, D.; Zhang, W.; Hu, J. Chalcogenide Glass Waveguide-Integrated Black Phosphorus Mid-Infrared Photodetectors. *J. Opt.* **2018**, *20*, 044004.
(37) Lin, H.; Song, Y.; Huang, Y.; Kita, D.; Deckoff-Jones, S.; Wang, K.; Li, L.; Li, J.; Zheng, H.; Luo, Z.; et al. Chalcogenide Glass-on-Graphene Photonics. *Nat. Photonics* **2017**, *11*, 798−805.
(38) Wang, Y.; Qiu, G.; Wang, Q.; Liu, Y.; Du, Y.; Wang, R.; Goddard, W. A.; Kim, M. J.; Ye, P. D.; Wu, W.; et al. Field-effect transistors made from solution-grown two-dimensional tellurene. *Nat. Electronics* **2018**, *1*, 228−236.
(39) Li, L.; Lin, H.; Huang, Y.; Shiue, R.-J.; Yadav, A.; Li, J.; Michon, J.; Englund, D.; Richardson, K.; Gu, T.; et al. High-Performance Flexible Waveguide-Integrated Photodetectors. *Optica* **2018**, *5*, 44.
(40) Guthmann, C.; Hermann, C.; Thuillier, J. M. Recombination Phenomena in Tellurium. *Phys. Status Solidi* **1970**, *3*, 365−374.
(41) *Infrared Detectors and Emitters: Materials and Devices*; Capper, P., Elliott, C. T., Eds.; Springer US: Boston, MA, 2001.
(42) Wang, R.; Muneeb, M.; Sprengel, S.; Boehm, G.; Malik, A.; Baets, R.; Amann, M.-C.; Roelkens, G. III-V-on-Silicon 2-Mm-Wavelength-Range Wavelength Demultiplexers with Heterogeneously Integrated InP-Based Type-II Photodetectors. *Opt. Express* **2016**, *24*, 8480.
(43) Wang, R.; Sprengel, S.; Muneeb, M.; Boehm, G.; Baets, R.; Amann, M.-C.; Roelkens, G. 2 Mm Wavelength Range InP-Based Type-II Quantum Well Photodiodes Heterogeneously Integrated on Silicon Photonic Integrated Circuits. *Opt. Express* **2015**, *23*, 26834.
(44) *Photonic Crystals: Molding the Flow of Light*; Joannopoulos, J. D., Johnson, S. G., Winn, J. N., Meade, R. D., Eds.; Princeton University Press, 2008.
(45) Lin, H.; Liu, J.; Hu, J.; Michel, J.; Zhang, L.; Ogbuu, O. Breaking the Energy-Bandwidth Limit of Electrooptic Modulators: Theory and a Device Proposal. *J. Lightwave Technol.* **2013**, *31* (24), 4029−4036.

DOI: 10.1021/acsphotonics.9b00694
ACS Photonics XXXX, XXX, XXX−XXX